Article

Admixture Effects on the Rheological/Mechanical Behavior and Micro-Structure Evolution of Alkali-Activated Slag Backfills

Xubo Ji [1,2], Xiaozhong Gu [1], Zhuoran Wang [1], Shuai Xu [1], Haiqiang Jiang [1,3],* and Erol Yilmaz [4],*

[1] Key Laboratory of Ministry of Education on Safe Mining of Deep Metal Mines, Northeastern University, Shenyang 110819, China
[2] Shandong Humon Smelting Co., Ltd., Yantai 264109, China
[3] Key Laboratory of Deep Coal Resource Mining, Ministry of Education, China University of Mining and Technology, Xuzhou 221116, China
[4] Department of Civil Engineering, Geotechnical Division, Recep Tayyip Erdogan University, Rize TR53100, Turkey
* Correspondence: jianghaiqiang@mail.neu.edu.cn (H.J.); erol.yilmaz@erdogan.edu.tr (E.Y.)

Abstract: Recently, alkali-activated slag (AAS) has attracted extensive attention in cemented paste backfill (CPB) due to its low cost/CO_2 emissions and high strength benefits. However, a comprehensive analysis of the mechanical/rheological behavior and microstructure evolution of AAS-CPB using mineral admixtures is still lacking. In this study, metakaolin (MK), fly ash (FA), and silica fume (SF) were employed to replace ground granulated blast furnace slag (GGBS) at various levels to formulate an alkali-activated binder, and the corresponding mechanical, rheological, and microstructure properties of CPB were investigated. The results suggest that FA tends to reduce CPB's rheological and strength evolution and this negative effect increases with the FA dosage. The replacement of MK or SF increases the rheological parameters and thus diminishes fluidity and has positive or negative effects on strength depending on the replacement level and curing age. This study's findings will contribute to developing a new scheme for lucrative and environmentally responsive multi-solid waste-based AAS-CPB in the field.

Keywords: cemented paste backfill; alkali-activated slag; mineral admixture; rheology; strength; microstructure

1. Introduction

Mining operations provide energy, building materials, and mineral-based raw materials necessary for the development of human society. However, mining waste, such as tailings, will be generated at the same time. Taking China as an example, the accumulation of tailings amounted to 22.2 billion tons by the end of 2020 [1], and the annual tailing emissions exceeded 1.5 billion tons, while the comprehensive utilization rate of tailings was only 18.9%. A large amount of tailing discharge will not only pollute the social environment, destroy the ecological balance, and cause accidents such as mudslides and dam failures [2–5] but will also destroy large amounts of terrestrial resources and hinder the economic development of enterprises. In addition, more underground goafs will be formed after mining activities, which can easily lead to falling roofs and surface collapse [6–10]. Therefore, dealing with the accumulation of tailings and underground goafs has become an urgent problem to be solved in underground mine operations.

Cementitious paste backfill (CPB) technology provides a new direction for solving the above problems [11–16]. CPB is an engineered composite material that typically contains tailings, binder agents, and mixing water [17,18]. CPB is transported by gravity/pipelines to mined-out goafs [19]. CPB can not only reduce tailing solid waste, solidified heavy metals, environmental pollution, and tailing pond management costs but can also significantly improve surface stability [20–23].

The binder plays a key role in CPB's properties such as strength, rheology, and microstructure [24–30]. Ordinary Portland cement (OPC) is one of the key cement types employed in mine fills due to its availability and versatility [31]. However, producing 1 ton of cement will release 800–1000 kg of CO_2 [32]. In addition, cement hydration produces significant heat, worsening the problem of high-temperature heat damage in deep mining. It is estimated that the binder prices represent approximately 75% of filling charges when OPC is used as a singular binder [33,34]. With growing concerns about the global greenhouse effect and sustainability issues, there is an urgent need for the backfill field to explore low-cost, wide-scale green cement alternatives. In recent years, alkali-activated cementitious materials have received extensive attention in the filling industry [35,36]. Compared to traditional Portland cement, alkali-activated cements have the advantages of low CO_2 emissions, high strength, good corrosion resistance, less hydration heat release, and low cost [37–39]. Alkali-activated cement materials seemingly have great prospects and potential as mine fill binders. Ground granulated blast furnace slag (GGBS), a type of built-up waste formed during iron/steel smelting progress at 1350–1450 °C, is one of the most prevalent choices as key raw products in the making of alkali-activated resources [40]. Compared to the hydration crops of OPC, those of alkali-activated slag (AAS) are lower in terms of their Ca/Si ratios, which contributes to the high strength/durability of samples.

Mineral admixtures have been utilized to improve workability, strength, and durability of cementitious material. Extensive studies have been conducted for enhancing rheological, mechanical, and durable properties. It is widely accepted that fly ash (FA) improves fluidity of cementitious slurries but decreases the early age strength due to its latent hydraulic properties [41]. Metakaolin (MK) is an amorphous alumina silicate produced by controlled thermal treatment of kaolin. MK could bring the following advantages: increased workability, improved strength, decreased permeability, and better acid attack, etc. [42]. Silica fume (SF) as an amorphous, highly reactive pozzolan has been recognized as a pozzolanic material for use as supplementary cementitious material to enhance mechanical and durability properties [43,44].

Numerous studies have been conducted to investigate the effect of mineral admixtures on the properties of AAS materials. For instance, Collins and Sanjayan [44] reported that partial replacement slag with 10% ultrafine FA in AAS concrete showed higher workability than neat AAS concrete. Messina et al. [45] explored the addition of GGBS, SF, and MK on early age performance of alkali-activated weathered fly ash and found that GGBS and MK were the most effective admixtures while SF failed to provide any performance improvement. Bernal et al. [46] concluded that alkali-activated slag/MK mortars gave higher strength than neat AAS mortar at silica modulus of 1.2 and 2. Rashad and Khalil [47] argued that the inclusion of SF in slag up to 15% enhanced the compressive strength, and the optimal content of SF that gave the highest compressive strength was 5%. However, these studies mainly focused on AAS paste, mortar, and concrete, which is significantly different from AAS-CPB in terms of their water–cement ratio, aggregate content, and activator concentration and silica modulus. Therefore, the findings of previous research cannot be directed implemented in AAS-CPB. In view of the above discussion, a comprehensive study of the influence of diverse admixture (mineral-based, not chemical, mixtures) substitution levels on the rheology, strength, and microstructure of AAS-CPB is necessary.

This study primarily explores rheological evolution, short-and long-term strength, ultrasonic behavior, and microporosity of CPB created with diverse mineral additive (e.g., FA, SF, and MK) substitution levels of GGBS. In addition, the changes in pore structure and hydration products under different curing times were scrutinized by both MIP (Hg intrusion porosimetry) experiments and SEM (scanning electron microscopy) observations. This paper is predominantly intended to offer an informative reference for the field implementation of AAS-CPB.

2. Materials and Methods

2.1. Materials

2.1.1. Tailings and Water

Artificial tailings (AT) were chosen for CPB preparation, with SiO_2 content accounting for more than 98% of total weight. Using AT instead of natural tailings can eliminate the influence of some active components on the test results. The grain size distribution of AT was obtained with a laser diffraction particle size analyzer (type Malvern Panalytical Mastersizer 2000), and the measured result is illustrated in Figure 1. Overall, 30.1% of AT had a grain diameter smaller than 20 μm. Here, AT have uniformity coefficient (C_u) and curvature coefficient (C_c) values of 17.28 and 1.80, respectively, which could be ordered to become well-graded. Table 1 presents the key physical characteristics of AT.
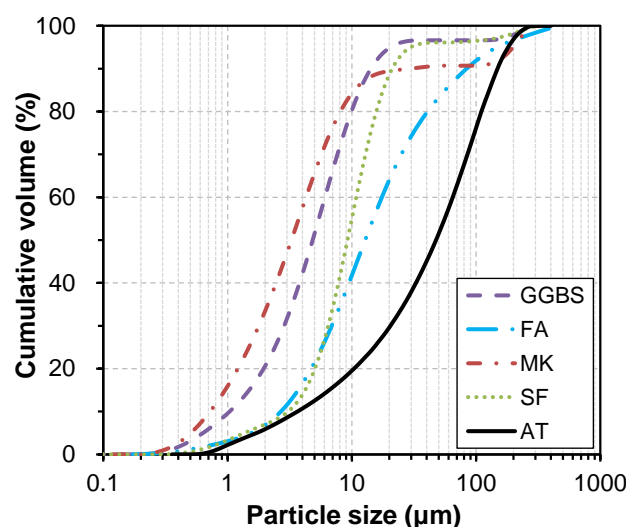

Figure 1. Grain size distribution curves of AT, GGBS, and mineral admixtures.

**Table 1.** Key physical properties of AT, GGBS, and mineral admixtures.

Type	D_{10} (μm)	D_{30} (μm)	D_{50} (μm)	D_{60} (μm)	D_{90} (μm)	Uniformity Coefficient	Curvature Coefficient	Specific Surface Area (m²/kg)	Specific Gravity (-)	28 d Pozzolanic Strength Index (%)
AT	3.71	20.7	48.7	64.1	147	17.28	1.80	117	2.73	-
GGBS	1.09	2.88	4.84	6.17	14.22	5.66	1.23	426	2.91	96.2
FA	2.87	7.01	12.83	16.13	52.83	6.21	1.01	322	2.01	68.7
MK	0.72	1.90	2.50	4.36	10.21	6.06	1.15	491	2.53	94.3
SF	2.94	6.51	9.22	12.08	21.12	4.1	1.32	21,054	2.17	88.4

2.1.2. Alkali-Activated GGBS

The GGBS used was provided by Wuhan Huashen Intelligent Technology Co., Ltd., and its particle size distribution is illustrated in Figure 1. Tables 1 and 2, respectively, present the physical and chemical characteristics of the studied materials. The principal components of GGBS are CaO (34.66%), SiO_2 (30.04%), Al_2O_3 (13.54%), MgO (7.07%), and Fe_2O_3 (7.07%). The XRD results in Figure 2 indicate that GGBS is mainly composed of calcium-silicon-rich glass, as well as a small amount of perovskite and fluorite. The alkali activator was created by proportionally mixing a sodium silicate solution (29.3% SiO_2, 12.7% Na_2O, and 58.0% H_2O) with sodium hydroxide (purity = 96%), providing a silica modulus of 0.34. Alkali activators were prepared and sealed 24 h before the test.

Table 2. The chemical structure of slag and mineral admixtures.

Chemical Composition (%)	GGBS	FA	MK	SF
Calcium oxide (CaO)	34.66	6.69	0.12	0.38
Silicon dioxide (SiO_2)	30.04	52.45	46.71	97.51
Aluminum oxide (Al_2O_3)	13.54	29.35	50.47	0.16
Magnesium oxide (MgO)	7.07	0.83	0.12	0.88
Ferric oxide (Fe_2O_3)	7.07	5.93	0.41	-
Potassium oxide (K_2O)	0.31	1.07	0.11	0.29
Sodium oxide (Na_2O)	0.33	0.89	0.28	0.33
Phosphorus pentoxide (P_2O_5)	-	0.24	0.38	0.25
Titanium oxide (TiO_2)	0.57	1.24	1.19	-
Sulfur trioxide (SO_3)	0.83	0.74	-	-
Manganese oxide (MnO_2)	0.13	-	-	-
Loss-on-ignition (LOI)	0.39	4.41	4.0	1.5
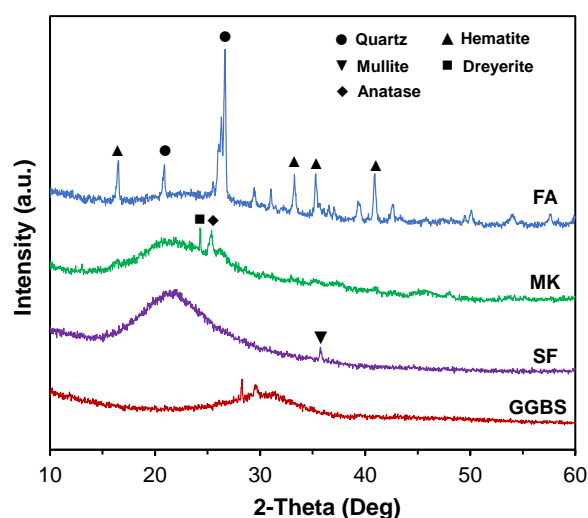
**Figure 2.** XRD results for GGBS and mineral admixtures.

2.1.3. Industrial Additives

FA, metakaolin (MK), and SF supplied by Wuhan Huashen Intelligent Technology Co., Ltd. (Wuhan, China) were used as industrial additives. MK had the smallest grain size, followed by GGBS, SF, and FA in ascending order (Figure 1). It should be noted that the grain size distribution of SF presented in Figure 1 is abnormally high, which is caused by the particle aggregation during the particle size measurement. Indeed, SF particles are extremely small and its specific surface area is almost 50 times that of GGBS. Table 1 lists the key physical characteristics of these mineral admixtures, while Table 3 lists the results for the key chemical compositions of FA, MK, and SF additives determined by X-ray fluorescence spectrometry (XRF). FA was mainly composed of SiO_2 (52.45%) and Al_2O_3 (29.35%), and, to a lesser extent, CaO (6.69%) and Fe_2O_3 (5.93%). The SiO_2 and Al_2O_3 contents in MK totaled 96%, while more than 97% of SF was SiO_2. The XRD analysis results presented in Figure 2 indicate that FA was mainly composed of hematite and quartz, while MK/SF was mainly shapeless as indicated by relatively broad XRD pattern peaks. Figure 3 illustrates the clear morphology of GGBS, FA, MK, and SF under SEM observations. Here, FA/SF presents a spherical morphology, while GGBS and MK appear as irregular flake particles.

Table 3. Details of the mix proportions.

Mix No.	Binder Proportions (%)				Binder Content $^{\alpha}$ (%)	Solid Concentration $^{\beta}$ (%)	Activator Concentration $^{\chi}$ (-)	Silica Modulus (-)
	Slag	Mineral Admixture						
		FA	MK	SF				
GGBS	100	0	0	0				
FA20	80	20	0	0				
FA40	60	40	0	0				
FA60	40	60	0	0				
MK5	95	0	5	0	10	77	0.3	0.34
MK15	85	0	15	0				
MK25	75	0	25	0				
SF5	95	0	0	5				
SF10	90	0	0	10				
SF15	85	0	0	15				

$^{\alpha}$ Solid concentration = $(W_{tailings} + W_{precursor})/W_{total} \times 100$; $^{\beta}$ Binder content = $W_{binder}/(W_{tailings} + W_{binder}) \times 100$; $^{\chi}$ Activator concentration = $W_{activator}/W_{binder}$.
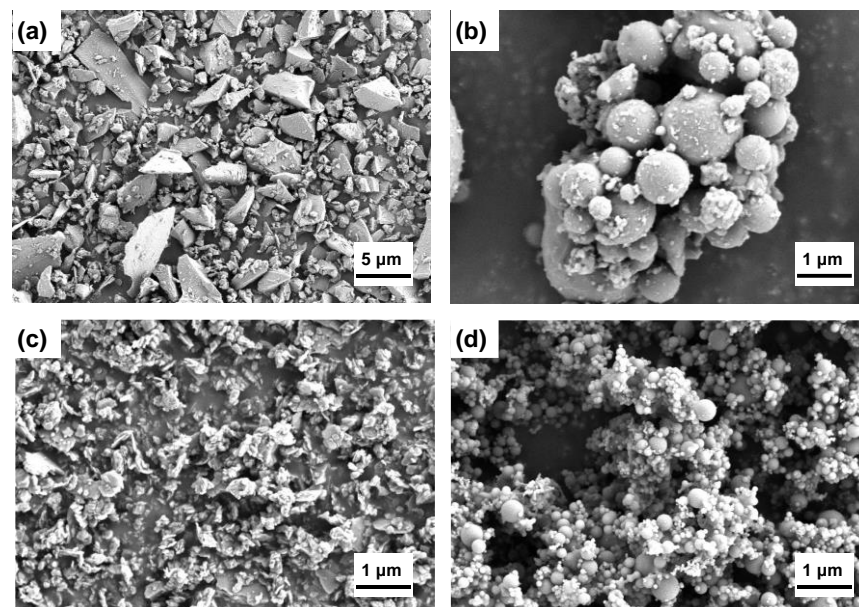
Figure 3. SEM micrographs of (**a**) GGBS; (**b**) FA; (**c**) MK; and (**d**) SF.

2.2. Sample Proportioning and Preparation

To explore the influence of mineral admixture on the rheology, strength, and microstructure evolution of AAS-CPB specimens, the GGBS was substituted with different percentages of FA, MK, and SF (20–60% for FA, 5–25% for MK, and 5–15% for SF). The adopted dosages of the mineral admixtures were determined through trial-and-error exploration. The solid concentration, silica modulus, and activator concentration were established constantly at 77%, 0.34%, and 0.3%, respectively, for all filling mixtures. These values were used because they gave the highest strength and adequate workability; their values were preliminarily determined to give favorable strength and sufficient fluidity. Before mixing, the tailings and precursors were weighted and thoroughly blended in dry form for 2 min. Activators were then cast in solids and blended by hand for an extra 2 min. Blending was carried out using a double-spiral mixer for 3 min. Then, the manufactured slurry composite was added to 5 cm × 10 cm sized molds and preserved within a curing box at 21 °C and 95% RH.

2.3. Methods of Investigation

2.3.1. Rheology Test

The rheological behavior of AAS-CPB slurries was measured using a Brookfield RST-CC rheometer equipped with a four-blade vane (diameter: 2 cm; height: 4 cm). The sequence of rheological measurements is illustrated in Figure 4 and can be summarized as follows:

- Insert the vane slowly down to the predetermined position in the slurry;
- Set the slurry for 30 s to eliminate the disturbance caused by the vane insertion;
- Increase the shearing rate from 0.001 to 100 s^{-1} within 1 min (up curve);
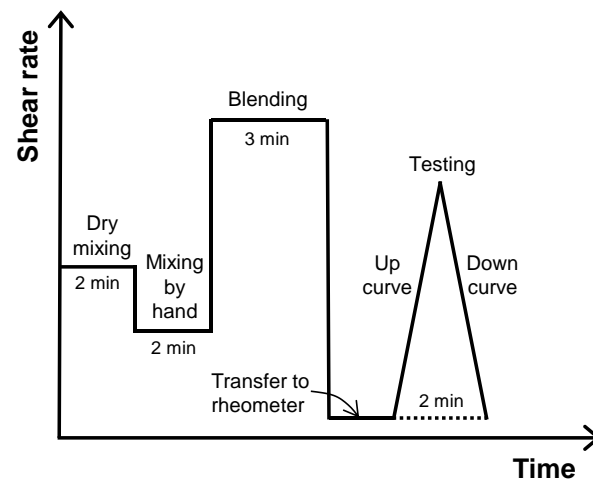- Decrease the shearing rate from 100 to 0.001 s^{-1} within 1 min (down curve).

Figure 4. A key flow chart of blending and rheological tests.

Considering the actual pipeline transportation time of the CPB slurry, rheological testing was performed at 0, 0.5, 1, and 2 h immediately after mixing. The data obtained from the descending curve were used to calculate the yield stress and plastic viscosity of AAS-CPB slurries. The Bingham model was chosen to linearly fit the rheological test data of the descending section since this model offers the best fit.

2.3.2. Uniaxial Compressive Strength (UCS) Test

A total of 5 time points (3, 7, 28, 56, and 90 days) were set for UCS testing. To determine the mechanical evolution of AAS-CPB specimens, a 50 kN loading capacity Humboldt HM-5030 press was utilized in the laboratory according to the ASTM C39/C39M-20 standard. The accuracy of the pressure sensor and displacement sensor were 0.0001 N and 0.0001 mm, respectively. The load was applied at 1 mm/min until specimen failure. Each UCS test was performed in triplicate, and the average value was recorded.

2.3.3. Ultrasonic Pulse Velocity (UPV) Test

This experiment has both geometric acoustic and physical acoustic characteristics. The structural composition and performance of the medium to be measured can be judged according to the differences of UPV in different media. The UPV of AAS-CPB was determined using a Proceq Pundit Lab ultrasound device (Schwerzenbach, Switzerland). This device offers a measurement range of 0.1–9999.9 μs with an accuracy of 0.1 μs. The tests were performed at 54 kHz as per ASTM C 597-16. Detailed procedures for UPV test can be found in [48].

2.3.4. Microstructural Analysis

Thermogravimetric (TG) analysis. To explore the shapes of the hydration materials, this analysis was conducted using a STA 449 F3 thermal analyzer (NETZSCH, Selb, Germany). Nitrogen was used as the atmosphere in the test, and the specimen was heated to

995 °C at a rate of 5 °C/min. The specimen used for the TG test was binder paste with a binder-to-water ratio of 1:1.

Scanning electron microscopy (SEM) observations. AAS-CPB specimen morphology was observed using a Gemini 300 (Zeiss, Göttingen, Germany). Before the test, the surface of the specimen was sputtered with gold to render it electrically conductive. The SEM testing was operated at an acceleration voltage of 5–15 kv and a magnification of 1000–5000 times.

Mercury intrusion porosimetry (MIP) test. The hardened AAS-CPB specimens' total porosity/pore size distribution was characterized by an Hg intrusion porosimeter (MicroActive AutoPore V 9600, Micromeritics Instrument Corp., Norcross, GA, USA) with a maximum injection pressure of 414 MPa. The experiment was carried out in two stages, i.e., a low-pressure stage (1.38 to 345 kPa) and a high-pressure stage (345 to 414 MPa), lasting 8 h each. Before microstructural analysis, the hardened binder paste and CPB samples were first submerged in ethanol to avoid hydrating the cement and then oven-dried at 45 °C until the specimen weight no longer changed.

3. Results and Discussion

3.1. Rheological Evolution

3.1.1. Effect of FA

Figure 5a,b presents the changes to the rheological factors of AAS-CPB specimens with varying contents of FA. It appears that the replacement of GGBS with an FA additive reduced the yield stress/plastic viscosity of AAS-CPB specimens because fly ash has much lower pozzolanic activity than GGBS and thus the amount of hydration products reduces with higher FA replacement [49]. Exchanging irregular angular-shaped GGBS with spherical-shaped FA could also diminish the contact between grains (the "ball bearing" effect) [50].
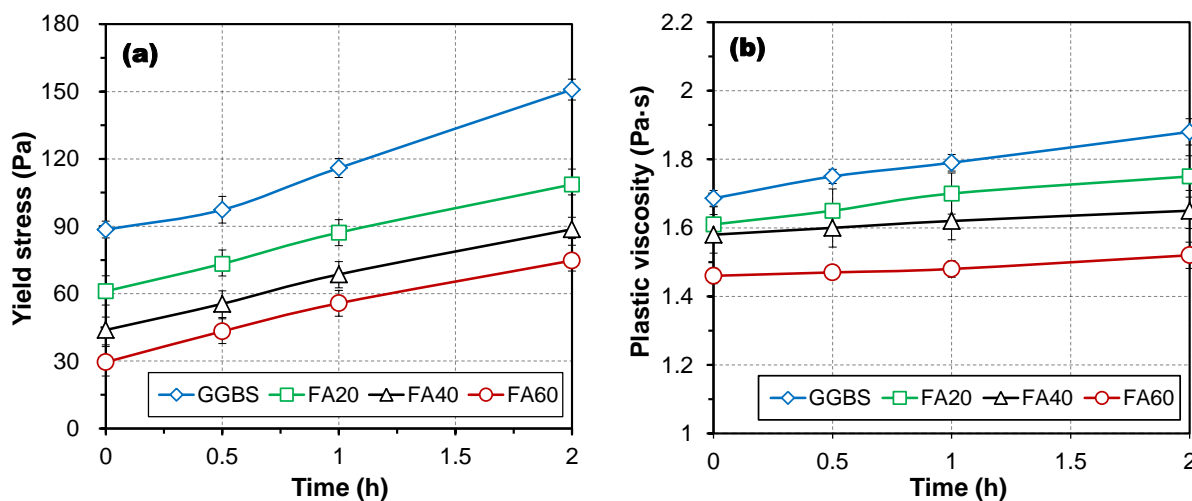

Figure 5. FA's effect on AAS-CPB yield stress (**a**) and plastic viscosity (**b**).

Similar conclusions were also reported in previous studies. Yang et al. [51] observed that fly ash microspheres significantly reduced the plastic viscosity of Na_2SiO_3-activated slag but had minimal positive or strong negative effects on yield stress depending on the silica modulus. However, a comparison of the curves in Figure 5a reveals that the positive influence of FA on yield stress diminishes with the replacement rate. To be specific, the initial 20% replacement leads to an average reduction of 27.3% in yield stress, while 22.1% and 19.3% reductions, on average, were observed, respectively, for the second and third 20% replacements. With replacement from 20% to 60%, the decrease in plastic viscosity was much smaller than the decrease in yield stress, indicating that FA has a greater effect on yield stress than plastic viscosity.

3.1.2. Effect of MK

Figure 6a,b shows MK's effect on the AAS-CPB's time-dependent rheological parameters. It is clear that AAS-CPBs with diverse contents of MK show similar trends in yield stress/plastic viscosity. Contrary to FA, adding MK causes a rise in yield stress/plastic viscosity; the higher replacement level is, the greater its negative impact becomes. Indeed, MK is much finer than GGBS (see Figure 1), and too much water is required to wet MK's surface, which reduces the amount of free water around the particles. Sonebi et al. [52] and Hamza et al. [53] also reported similar results for traditional cement-based materials. Another possible explanation is that Al and Si ions resolved from MK change the chemical characteristics of the particles and pore water chemistry, which can significantly influence the magnitude of the various inter-particle forces and the viscosity of fluid [54].
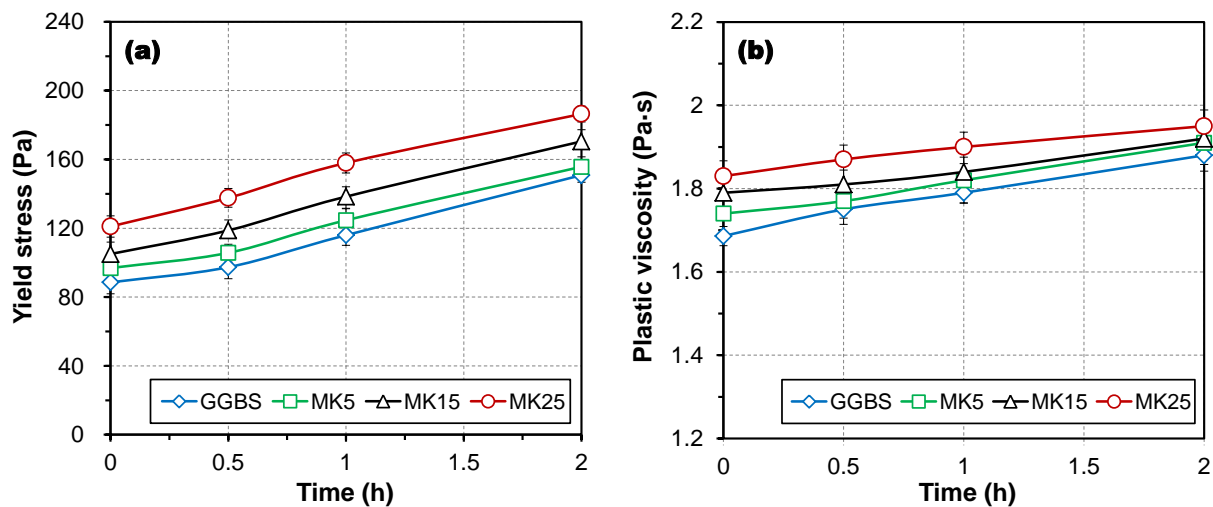

Figure 6. Evolution of MK-containing slurries' yield stress (**a**) and viscosity (**b**) over time.

Figure 6a,b shows that the addition of 5%, 15%, and 25% MK causes, on average, a 7.2%, 18.2%, and 34.5% increase in yield stress, respectively, while the corresponding increase in plastic viscosity is 1.90%, 3.6% and 6.3%. This difference in the increasing rate between yield stress and viscosity suggests that adding MK is more effective in growing yield stress than viscosity.

3.1.3. Effect of SF

Figure 7a,b indicates the growth of rheological factors of AAS-CPB specimens with varying contents of SF. Similar to MK, SF's presence increases the rheological parameters of AAS-CPB specimens, and this increase is positively related to the replacement rate. Although SF and FA are both spherical, SF has a much larger surface area than FA. Hence, a higher level of GGBS replacement with SF means a smaller amount of free water and, consequently, a closer mean distance between particles. Furthermore, the silica-rich SF can hydrate in the alkali environment and produces secondary hydration products characterized by high surface area, leading to an increase in the rheological parameters.

Meanwhile, when no additional water is added or a water-reducing agent is used, SF particles cannot be uniformly dispersed in the system and act as a filler to achieve the above-mentioned "bearing effect" [55]. Thus, when using SF and MK as the mineral admixtures in actual practice, more water or the use of water-reducing agents is required [56,57].

Figure 7a shows that the addition of an initial 5% SF gave rise to a 34.66% growth in yield stress, while only 6.66% and 9.4% increases, respectively, were observed for the second and third 5% additions. When 5%, 10%, and 15% SF were added, the apparent viscosity increased by 15.5 %, 9.9%, and 9.0%, respectively, which was much higher than that caused by the addition of MK.
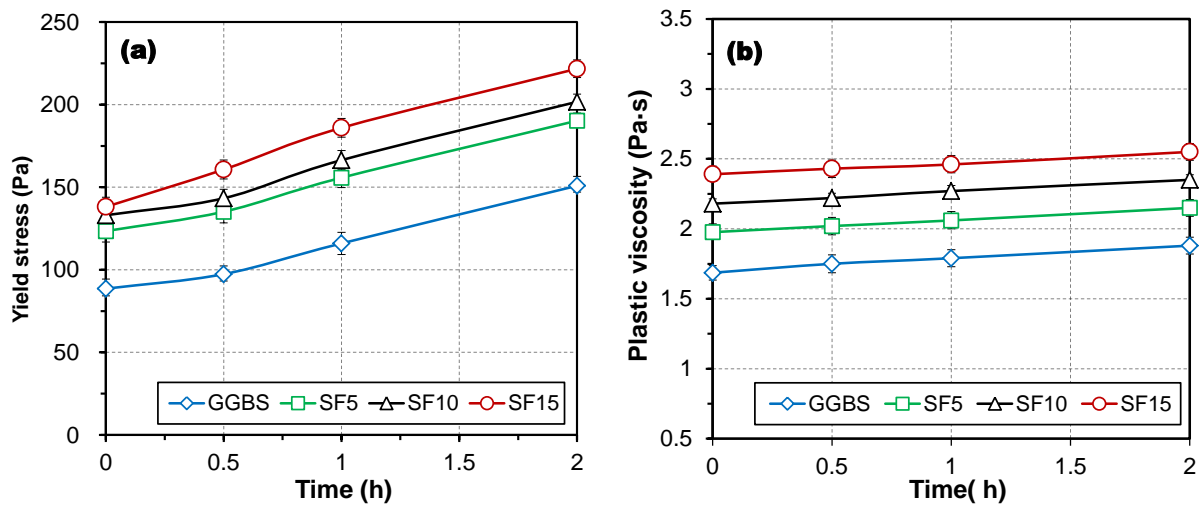
Figure 7. Evolution of time-dependent yield stress (**a**) and viscosity (**b**) of AAS-CPB specimens with diverse SF amounts.

3.2. Mechanical Strength

3.2.1. Effect of FA

Figure 8 presents FA's effects on AAS-CPB's strength development. Here, irrespective of the rate of FA replacement, the strength of all specimens grew with an increase in age. This occurred because as hydration of the binder proceeded, the aluminosilicate gel phase continuously formed. These gels precipitated and filled voids between grains, making the AAS-CPB specimen stiffer. The strength of all specimens increased rapidly during the initial 28 d, but then the rate of gain in strength slowed down. For instance, at a 20% replacement level, the increase during the initial 28 d was about 133.3%, and the increase from 28 to 90 d reduced to only 23.72%.
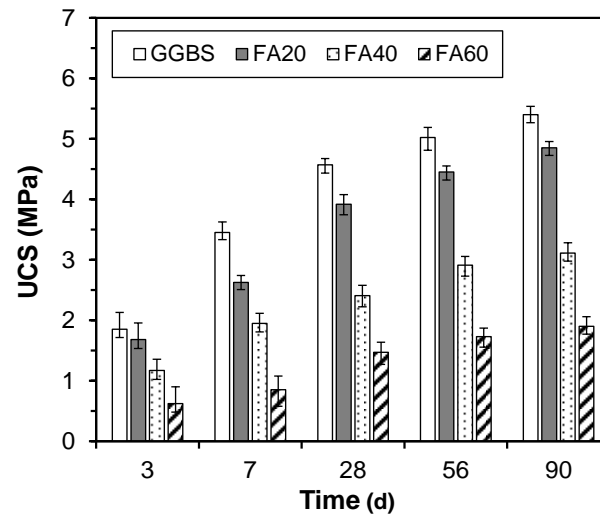

Figure 8. FA's effect on AAS-CPB's strength development.

Substituting GGBS with FA yielded a major drop in specimen strength acquisition; the greater the replacement amount was, the higher magnitude of the degradation became, as was reported by [58,59]. To explore FA in the hydration products of AAS-CPB specimens, a TG analysis was carried out on the samples cured for 28 d, and the results are summarized in Figure 9.
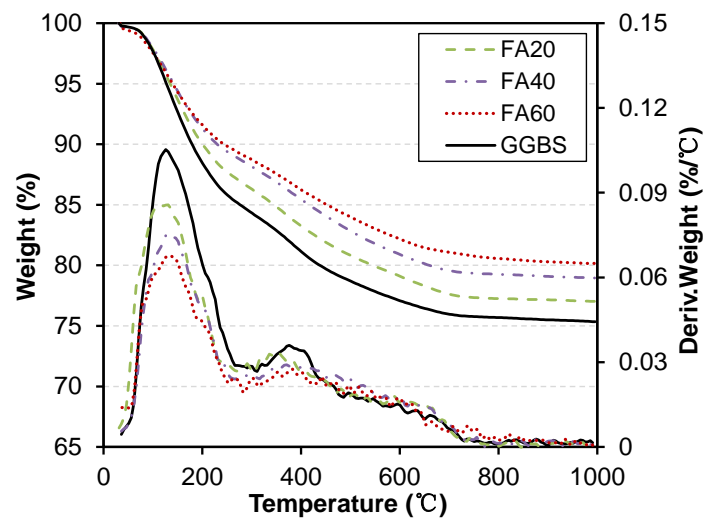
Figure 9. TG/DTG of GGBS, FA20, FA40, and FA60 pastes at 28 d.

Clearly, there are two main peaks (weight losses) in the curves. The mass loss at 100–400 °C is supported by the dehydration of AFt, AFm, and CSH gel, while the other loss around 400 °C resulted from the dehydroxylation of portlandite [60]. In the AAS system, the amount of AFt and AFm formed was negligible. As shown in Figure 9, as the rate of FA increased, the first peak dropped gradually, indicating a smaller amount of hydration products. Comparable conclusions for AAS mortar and concrete were also reported by Alanazi et al. [61] and Kumar et al. [58].

3.2.2. Effect of MK

Figure 10 presents MK's effect on strength increases of AAS-CPB. Substituting GGBS with MK produced a positive or negative impact on AAS-CPB's strength based on the rate of replacement and age. The addition of MK at low (5%) and medium (15%) levels slightly improved AAS-CPB's strength up to 56 days, and higher MK contents were associated with greater improvements in strength. This is because finer MK particles can fill the void within the AAS-CPB matrix and, therefore, make the microstructure denser. In addition, aluminum- and silica-rich MK reacts relatively rapidly in an alkaline environment and generates C(N)-A-S-H gels with higher Si/Ca and Al/Ca ratios [62–66].
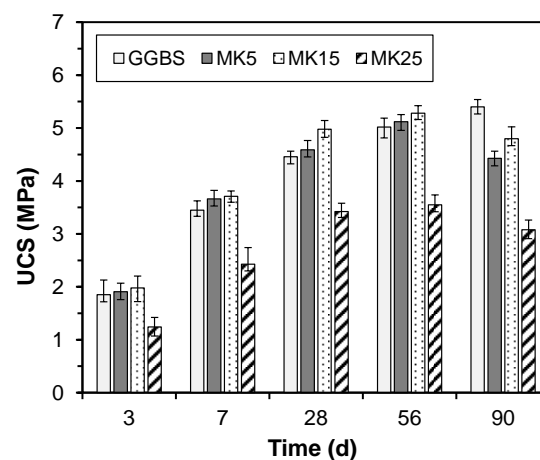

Figure 10. MK's effect on AAS-CPB's strength development.

The latter explanation is in concordance with the results of the SEM-EDX analysis of 56-day-aged AAS samples with 0% and 15% MK additives (Figure 11). The results presented in Figure 11 indicates that both Si/Ca and Al/Ca ratio of the C(N)-A-S-H gels

for the specimen with 15% MK was much higher than those for the sample with only GGBS. Susan et al. [62] explored MK's effects on the strength of AAS-based concrete with high alkalinity and observed that 10% MK incorporation leads to increased early aged (28-day) strength. Unexpectedly, the strength of the filling specimens with 5% and 15% MK additives experienced significant degradation from 56 to 90 days, resulting in a lower strength than that of the sample without MK. The mechanism for this behavior is outside the scope of this work and will be explored in our future research.
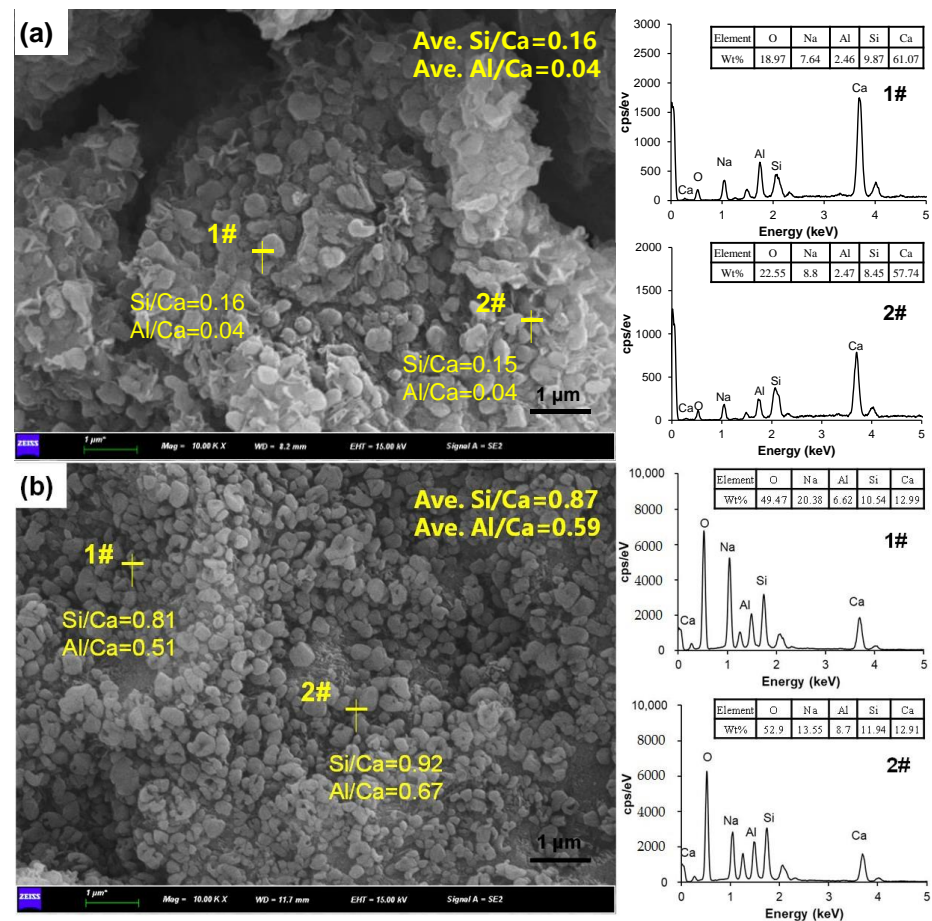

Figure 11. SEM-EDS results of 56-day-aged binder pastes prepared with (**a**) 0% MK and (**b**) 15% MK.

Unlike the effects of MK at 5% and 15% replacement levels, the 25% incorporation of MK significantly reduced the strength increases of all aged AAS-CPB specimens. Similar findings were also observed for AAS paste [62]. The authors attributed this reduction in strength under the incorporation of high MK content to the incomplete reaction of the MK. Similarly, Burciaga-Díaz et al. [67] found that for AAS prepared with only GGBS, 5% Na_2O can make it reach maximum strength, while a tripling of Na_2O content is needed for the sample with 50% MK to achieve the same strength. As with the samples including 5% and 15% MK, AAS-CPB with 25% MK also showed an obvious degradation in strength.

3.2.3. Effects of SF

Figure 12 indicates that the strength behavior of all specimens is similar: the strength gain at 3–28 days was fastest, while the growth rate at 28–90 days was a slower increase. When the SF dosage increased from 5% to 15%, the growth rates were 153.2%, 139.44%, and 130.7%, respectively. The slow growth rate was 12.53%, 10.5%, and 8.93%, respectively. Similar to the case of MK, adding SF also led to an increase or decrease within the filling specimens' strength, depending on the dosage. The strength of the samples with low SF content (5%) was always higher than that of the control. For instance, at a curing age of

28 days, the strength difference reached 12.47%. This positive effect of SF substitution on strength can be attributed to the filling and/or nucleation effect of SF, which produces a finer microstructure and less porosity. Moreover, the silica-rich SF also contributes to the formation of additional aluminosilicate gels with lower Ca/Si. Therefore, the strength will be enhanced at 5% replacement level. The experimental conclusion is also consistent with the results of the studies conducted by Rostami [68] and Ramezanianpou [69].
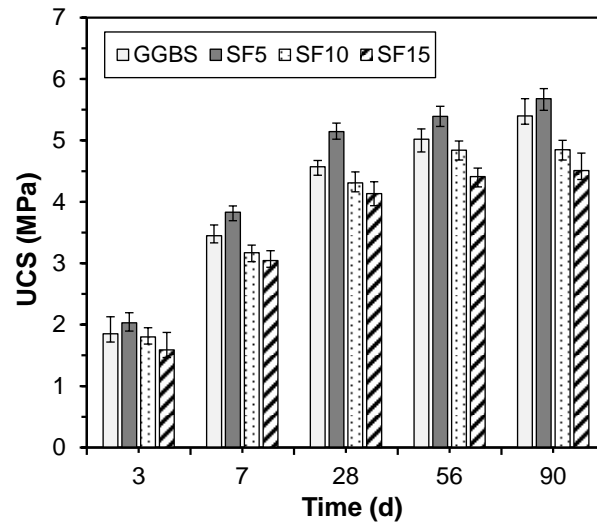

Figure 12. SF's effect on CPB's strength properties.

However, when the addition was 10% and 15%, the mechanical performance was weaker than that of the control. The strength depression was more obvious when the SF dosage increased from 10% to 15%. Compared to the pure GGBS group, the largest strength difference was in the test group with a curing age of 90 day, corresponding to 10.18% and 16.48% decreases in strength, respectively. This is because SF is less active than GGBS under alkaline conditions and thus excessive SF addition will lead to a smaller amount of hydration products. This decrease in the amount of hydration products means a higher porosity and coarser microstructure. To verify the above statement, MIP tests were done to characterize the pore structures of the 28-day-aged GGBS SF5 and SF10 specimens. Adding 5% SF produced a filler effect and formed a compact microstructure in coordination with slag (Figure 13). However, the sample with 10% SF showed a coarser pore structure compared to the samples made with 0% SF and 5% SF.
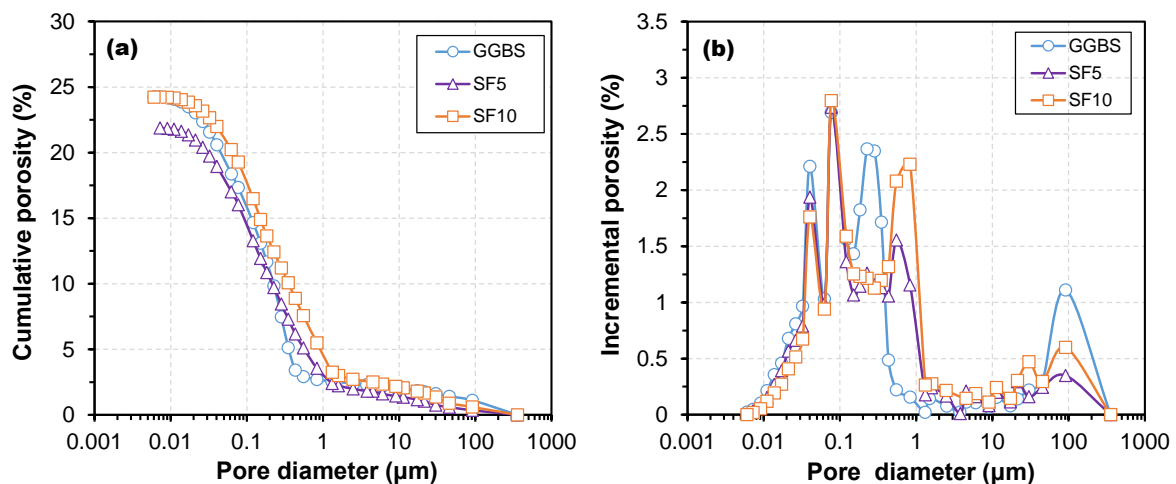

Figure 13. Cumulative (**a**) and incremental (**b**) MIP results of 28-day-aged GGBS, SF5, and SF10.

Similar observations were made on odium silicate-based alkali-activated slag/glass powder (AASG) pastes by Li et al. [70]. These authors attributed the decreased strength with SF higher than 15% to the increased amount of large capillary pores. Moreover, Dutta et al. [49] established that adding up to 5% SF to FA admixture yields an increase in strength; however, additional additions will cause a decrease. A good approach to conducing strength increases of filling specimens with large SF rates is to increase the curing temperature. During curing, high temperatures will also hasten the reaction of cement hydration, counteracting the negative effects of SF on strength. The curing temperature in this study was 20 ± 1 °C, so when the SF replacement level was excessive, the strength naturally decreased.

3.3. Ultrasonic Property

Figure 14 shows the ultrasonic pulse velocity (UPV) of AAS-CPBs with FA/MK/SF admixtures as a function of curing age. A comparison of the UPV (Figure 14) and strength (Figure 8, Figure 10, and Figure 12) results revealed that the UPV of AAS-CPBs, irrespective of mineral admixture type, exhibited trends almost similar to those of strength. The UPV increased rapidly during the first 28 days yet increased more slowly from 28 to 90 days because the degree of hydration reaction decreased in later stages, stabilizing the microstructure of the CPB.
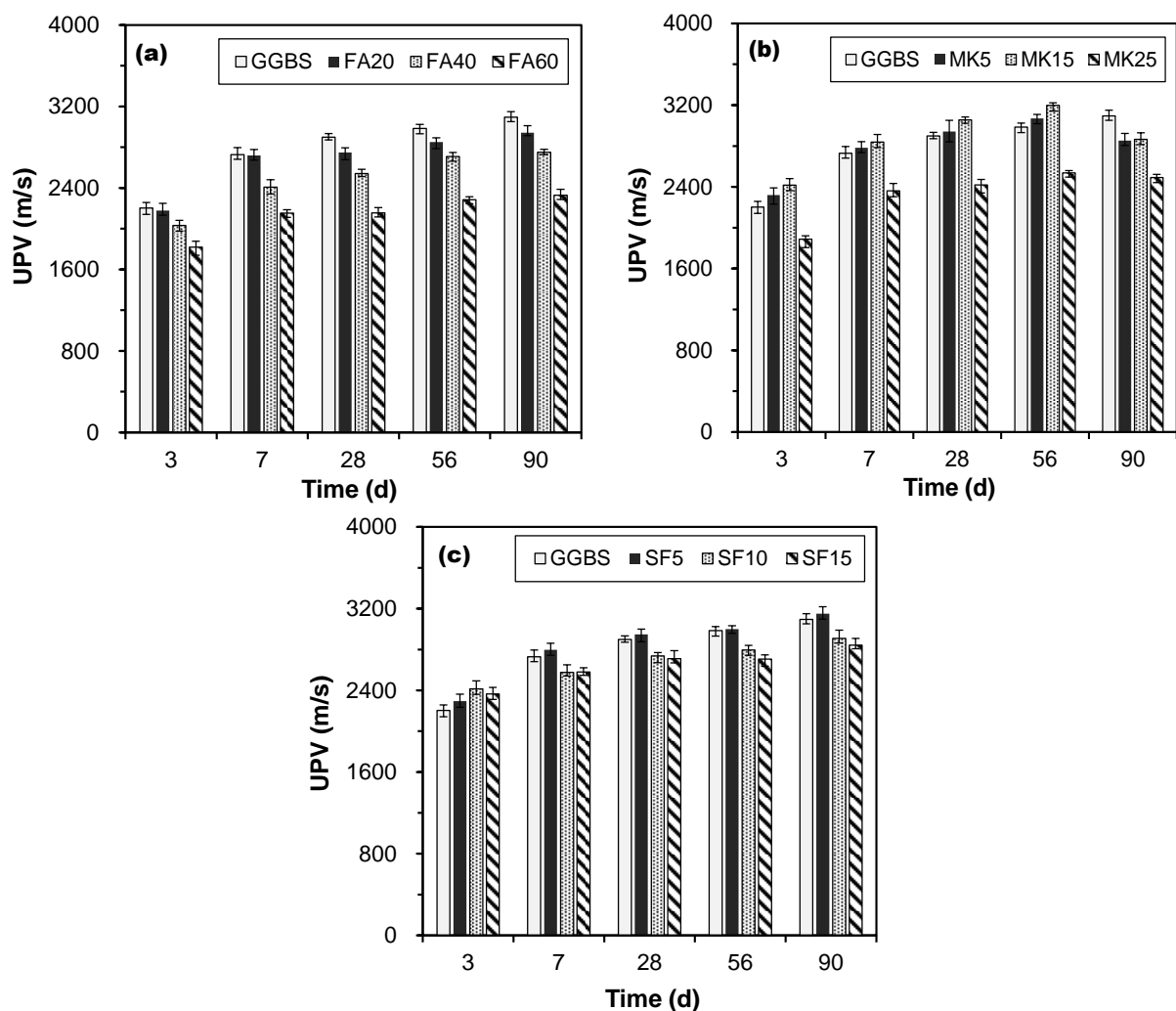

Figure 14. (**a**) UPV results of AAS-CPB containing (**a**) FA; (**b**) MK; and (**c**) SF.

Several works have sought to explore the link between the UCS and UPV of filling specimens. Some studies [48,71–74] on cement-based CPB suggest a strong linear link

between UCS and UPV. Nevertheless, plotting the UCS-UPV performance of AAS-CPB specimens reveals a nonlinear and/or exponential curve [75]. To explore the link between UCS and UPV for AAS-CPB specimens with admixtures, we plotted strength vs. equivalent ultrasonic values (Figure 15). Diverse regression types (linear, logarithmic, exponential, power, and polynomial) were used to obtain the most suitable link between UCS and UPV. Linear curves with correlation coefficients larger than 0.9 were found to best represent the link between the UCS and UPV of AAS-CPB, irrespective of mineral admixture type.
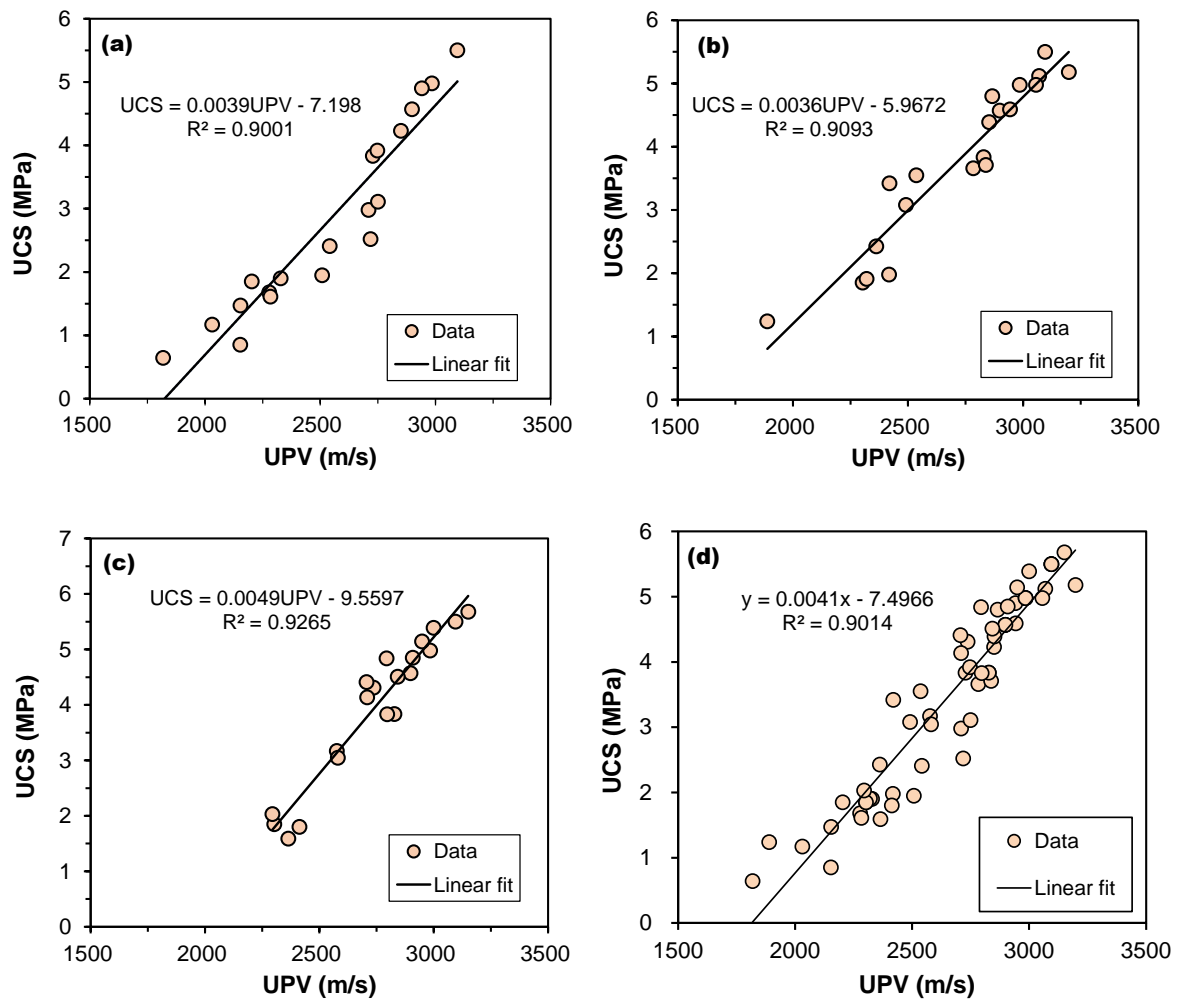

Figure 15. Links between UCS and UPV for AAS-CPB with (**a**) FA; (**b**) MK; (**c**) SF; and (**d**) all.

To verify the implication of linear relations, *t*- and *F*-tests were performed (Table 4). A 95% level of confidence was chosen. The estimated t- and F-values were larger than the equivalent tabulated ones for all mixtures, indicating that all the models are valid. These findings indicate that the strength of AAS-CPB with mineral admixture can be predicted using a UPV test.

Table 4. Results of the *t*- and *F*-test.

Mixtures	Mineral Admixture	$t_{computed}$	$t_{tabulated}$	$F_{computed}$	$F_{tabulated}$
All specimens	FA, MK, SF	18.36877	2.002	121.65934	1.662
AAS-CPB with FA	FA	8.10443	2.093	42.2938	2.168
AAS-CPB with MK	MK	12.59867		31.69466	
AAS-CPB with SF	SF	13.27459		32.35564	

4. Conclusions

In this study, a mixture of NaOH/Na$_2$SiO$_3$ was employed as a basic activator, and different contents of FA (20%, 40%, and 60%), MK (5%, 15%, and 25%), and SF (5%, 10%, and 15%) were added as a substitute for slag in further tests, including rheology, UCS, and UPV experiments. In addition, TG, SEM, and MIP experiments were undertaken to explore the influence of the type and replacement level of mineral admixtures on the AAS system. The resulting conclusions are as follows:

- Adding FA will reduce the rheological parameters of fresh AAS-CPB and improve fluidity; the larger the replacement amount, the more obvious the improvement effect. However, FA will also decrease the UCS of specimens due to the reduction of CSH in the system.
- As a result of the finer grain size of MK compared to slag, the partial replacement of slag with MK will increase the yield stress and viscosity of fresh AAS-CPB. Slag replacement amounts of 5% and 15% offered an early gain in strength but were detrimental to later strength. This result was attributed to the low gel strength of the admixture caused by Al-rich MK.
- SF will pointedly reduce the rheological evolution of AAS-CPB due to its high specific surface, but at the same time, a small amount of substitution (5%) will also enhance the strength of the specimen. A further increase in SF content will reduce the filling's strength.
- Replacing GGBS with MK and SF can cause a change in the pore water chemistry, surface chemistry of the particles, and the composition of hydrates, resulting in a variation in the rheological and mechanical properties.
- A linear relationship between the UCS and UPV of AAS-CPB is obtained irrespective of mineral admixture type. The UPV test provides one reliable and accurate way to predict the strength of AAS-CPB with mineral admixtures.

Author Contributions: Conceptualization, H.J. and E.Y.; methodology, X.G.; validation, Z.W and X.G.; formal analysis, S.X.; investigation, X.J.; resources, X.J.; data curation, Z.W.; writing—original draft preparation, X.J.; writing—review and editing, H.J. and E.Y.; visualization, Z.W.; supervision, S.X.; project administration, H.J.; funding acquisition, S.X. All authors have read and agreed to the published version of the manuscript.

Data Availability Statement: Not applicable.

References

1. Wei, M.; Kong, X.; Huang, J. Current status and suggestions for the disposal of tailing waste in China. *Chem. Miner. Process.* **2022**, *5*, 34–38. [CrossRef]
2. Tiwary, R.K. Environmental Impact of Coal Mining on Water Regime and Its Management. *Water Air Soil Pollut.* **2001**, *132*, 185–199. [CrossRef]
3. Bell, F.G.; Stacey, T.R.; Genske, D.D. Mining subsidence and its effect on the environment: Some differing examples. *Environ. Geol.* **2000**, *40*, 135–152. [CrossRef]
4. Kesimal, A.; Yilmaz, E.; Ercikdi, B.; Alp, I.; Deveci, H. Effect of properties of tailings and binder on the short-and long-term strength and stability of cemented paste backfill. *Mater. Lett.* **2005**, *59*, 3703–3709. [CrossRef]
5. Chen, Q.; Tao, Y.; Feng, Y.; Zhang, Q.; Liu, Y. Utilization of modified copper slag activated by Na(2)SO(4) and CaO for unclassified lead/zinc mine tailings based cemented paste backfill. *J. Environ. Manag.* **2021**, *290*, 112608. [CrossRef] [PubMed]
6. Li, W.; Mamadou, F. Strength and self-desiccation of slag-cemented paste backfill at early ages: Link to initial sulphate concentration. *Cem. Concr. Compos.* **2018**, *89*, 160–168. [CrossRef]
7. Qiu, J.; Yang, L.; Xing, J.; Sun, X. Analytical Solution for Determining the Required Strength of Mine Backfill Based on its Damage Constitutive Model. *Soil Mech. Found. Eng.* **2018**, *54*, 371–376. [CrossRef]
8. Zhang, S.; Ren, F.; Zhao, Y.; Qiu, J.; Guo, Z. The effect of stone waste on the properties of cemented paste backfill using alkali-activated slag as binder. *Constr. Build. Mater.* **2021**, *283*, 122686. [CrossRef]

9. Cihangir, F.; Ercikdi, B.; Kesimal, A.; Ocak, S.; Akyol, Y. Effect of sodium-silicate activated slag at different silicate modulus on the strength and microstructural properties of full and coarse sulphidic tailings paste backfill. *Constr. Build. Mater.* **2018**, *185*, 555–566. [CrossRef]

10. Cihangir, F.; Ercikdi, B.; Kesimal, A.; Deveci, H.; Erdemir, F. Paste backfill of high-sulphide mill tailings using alkali-activated blast furnace slag: Effect of activator nature, concentration and slag properties. *Miner. Eng.* **2015**, *83*, 117–127. [CrossRef]

11. Yin, S.; Shao, Y.; Wu, A.; Wang, H.; Liu, X.; Wang, Y. A systematic review of paste technology in metal mines for cleaner production in China. *J. Clean. Prod.* **2020**, *247*, 119590. [CrossRef]

12. Yin, S.; Shao, Y.; Wu, A.; Wang, Z.; Yang, L. Assessment of expansion and strength properties of sulfidic cemented paste backfill cored from deep underground stopes. *Constr. Build. Mater.* **2020**, *230*, 116983. [CrossRef]

13. Yin, S.; Shao, Y.; Wu, A.; Wang, Y.; Chen, X. Expansion and strength properties of cemented backfill using sulphidic mill tailings. *Constr. Build. Mater.* **2018**, *165*, 138–148. [CrossRef]

14. Chen, Q.; Sun, S.; Liu, Y.; Qi, C.; Zhou, H.; Zhang, Q. Immobilization and leaching characteristics of fluoride from phosphogypsum-based cemented paste backfill. *Int. J. Miner. Metall. Mater.* **2021**, *28*, 1440–1452. [CrossRef]

15. Wang, Y.; Wang, Z.; Wu, A.; Wang, L.; Na, Q.; Cao, C.; Yang, G. Experimental research and numerical simulation of the multi-field performance of cemented paste backfill: Review and future perspectives. *Int. J. Miner. Metall. Mater.* **2023**, *30*, 193–208. [CrossRef]

16. Qi, C.; Fourie, A. Cemented paste backfill for mineral tailings management: Review and future perspectives. *Miner. Eng.* **2019**, *144*, 106025. [CrossRef]

17. Wang, X.; Wang, X.; Shi, X. Modification of carbonate-activated binder for lead-zinc mine tailings based cemented paste backfill. *Constr. Build. Mater.* **2022**, *326*, 126871. [CrossRef]

18. Ouffa, N.; Trauchessec, R.; Benzaazoua, M.; Lecomte, A.; Belem, T. A methodological approach applied to elaborate alkali-activated binders for mine paste backfills. *Cem. Concr. Compos.* **2022**, *127*, 104381. [CrossRef]

19. Simon, D.; Grabinsky, M. Apparent yield stress measurement in cemented paste backfill. *Int. J. Min. Reclam. Environ.* **2013**, *27*, 231–256. [CrossRef]

20. Chen, Q.; Zhu, L.; Wang, Y.; Chen, J.; Qi, C. The carbon uptake and mechanical property of cemented paste backfill carbonation curing for low concentration of CO_2. *Sci. Total Env.* **2022**, *852*, 158516. [CrossRef]

21. Chen, Q.; Luo, K.; Wang, Y.; Li, X.; Zhang, Q.; Liu, Y. In-situ stabilization/solidification of lead/zinc mine tailings by cemented paste backfill modified with low-carbon bentonite alternative. *J. Mater. Res. Technol.* **2022**, *17*, 1200–1210. [CrossRef]

22. Yan, B.; Jia, H.; Yilmaz, E.; Lai, X.; Shan, P.; Hou, C. Numerical study on microscale and macroscale strength behaviors of hardening cemented paste backfill. *Constr. Build. Mater.* **2022**, *321*, 126327. [CrossRef]

23. Cihangir, F.; Ercikdi, B.; Kesimal, A.; Turan, A.; Deveci, H. Utilisation of alkali-activated blast furnace slag in paste backfill of high-sulphide mill tailings: Effect of binder type and dosage. *Miner. Eng.* **2012**, *30*, 33–43. [CrossRef]

24. Yin, S.; Wu, A.; Hu, K.; Wang, Y.; Zhang, Y. The effect of solid components on the rheological and mechanical properties of cemented paste backfill. *Miner. Eng.* **2012**, *35*, 61–66. [CrossRef]

25. Liu, L.; Xin, J.; Huan, C.; Zhao, Y.-J.; Fan, X.; Guo, L.-J.; Song, K.-I. Effect of curing time on the mesoscopic parameters of cemented paste backfill simulated using the particle flow code technique. *Int. J. Miner. Metall. Mater.* **2021**, *28*, 590–602. [CrossRef]

26. Zhang, Q.; Wu, H.; Feng, Y.; Wang, D.; Su, H.; Li, X. Rheological and physicomechanical properties of rod milling sand-based cemented paste backfill modified by sulfonated naphthalene formaldehyde condensate. *Int. J. Miner. Metall. Mater.* **2023**, *30*, 225–235. [CrossRef]

27. Wu, A.; Ruan, Z.; Wang, J. Rheological behavior of paste in metal mines. *Int. J. Miner. Metall. Mater.* **2022**, *29*, 717–726. [CrossRef]

28. Qi, C.; Ly, H.; Yang, X.; Guo, L.; Thai Pham, B. Improved strength prediction of cemented paste backfill using a novel model based on adaptive neuro fuzzy inference system and artificial bee colony. *Constr. Build. Mater.* **2021**, *284*, 122857. [CrossRef]

29. Cao, S.; Zheng, D.; Yilmaz, E.; Yin, Z.; Xue, G.; Yang, F. Strength development and microstructure characteristics of artificial concrete pillar considering fiber type and content effects. *Constr. Build. Mater.* **2020**, *256*, 119408. [CrossRef]

30. Li, J.; Cao, S.; Yilmaz, E.; Liu, Y. Compressive fatigue behavior and failure evolution of additive fiber-reinforced cemented tailings composites. *Int. J. Miner. Metall. Mater.* **2022**, *29*, 345–355. [CrossRef]

31. Tariq, A.; Yanful, E.K. A review of binders used in cemented paste tailings for underground and surface disposal practices. *J. Environ. Manag.* **2013**, *131*, 138–149. [CrossRef] [PubMed]

32. Yang, K.; Cho, A.; Song, J.; Nam, S. Hydration products and strength development of calcium hydroxide-based alkali-activated slag mortars. *Constr. Build. Mater.* **2012**, *29*, 410–419. [CrossRef]

33. McCaffrey, R. Climate Change and the Cement Industry. *Glob. Cem. Lime Mag. (Environ. Spec. Issue)* **2002**, 15–19.

34. Zhou, N.; Dong, C.; Zhang, J.; Meng, G.; Cheng, Q. Influences of mine water on the properties of construction and demolition waste-based cemented paste backfill. *Constr. Build. Mater.* **2021**, *313*, 125492. [CrossRef]

35. Pacheco-Torgal, F.; Castro-Gomes, J.; Jalali, S. Alkali-activated binders: A review: Part 1. Historical background, terminology, reaction mechanisms and hydration products. *Constr. Build. Mater.* **2008**, *22*, 1305–1314. [CrossRef]

36. Xue, G.; Yilmaz, E.; Song, W.; Cao, S. Compressive Strength Characteristics of Cemented Tailings Backfill with Alkali-Activated Slag. *Appl. Sci.* **2018**, *8*, 1537. [CrossRef]

37. Edmeades, R.M.; Hewlett, P.C. 15-Cement Admixtures. In *Lea's Chemistry of Cement and Concrete*, 4th ed.; Hewlett, P.C., Ed.; Butterworth-Heinemann: Oxford, UK, 1998; pp. 841–905. [CrossRef]

38. Patzelt, N.D. Finish grinding of slag. *World Cem.* **1993**, *24*, 51–58.

39. Committee, A.C.I. Ground Granulated Blast-Furnace Slag as a Cementitious Constituent in Concrete. *ACI Mater. J.* **1987**, *84*, 327–342. [CrossRef]

40. Ismail, I.; Bernal, S.A.; Provis, J.L.; San Nicolas, R.; Hamdan, S.; van Deventer, J.S.J. Modification of phase evolution in alkali-activated blast furnace slag by the incorporation of fly ash. *Cem. Concr. Compos.* **2014**, *45*, 125–135. [CrossRef]

41. Mehta, P.K.; Monteiro, P.J.M. *Concrete: Microstructure, Properties, and Materials*; MC Graw Hill India: New York, NY, USA, 2005.

42. Vivek, S.S.; Dhinakaran, G. 18-Strength and microstructure properties of self-compacting concrete using mineral admixtures. Case study I. In *Handbook of Sustainable Concrete and Industrial Waste Management*; Colangelo, F., Cioffi, R., Farina, I., Eds.; Woodhead Publishing: Sawston, UK, 2022; pp. 387–405. [CrossRef]

43. Siddique, R.; Kunal; Mehta, A. 11-Utilization of industrial by-products and natural ashes in mortar and concrete development of sustainable construction materials. In *Nonconventional and Vernacular Construction Materials*, 2nd ed.; Harries, K.A., Sharma, B., Eds.; Woodhead Publishing: Sawston, UK, 2020; pp. 247–303. [CrossRef]

44. Collins, F.; Sanjayan, J.G. Effects of ultra-fine materials on workability and strength of concrete containing alkali-activated slag as the binder. *Cem. Concr. Res.* **1999**, *29*, 459–462. [CrossRef]

45. Messina, F.; Ferone, C.; Colangelo, F.; Cioffi, R. Low temperature alkaline activation of weathered fly ash: Influence of mineral admixtures on early age performance. *Constr. Build. Mater.* **2015**, *86*, 169–177. [CrossRef]

46. Bernal, S.A.; Provis, J.L.; Rose, V.; Mejía de Gutierrez, R. Evolution of binder structure in sodium silicate-activated slag-metakaolin blends. *Cem. Concr. Compos.* **2011**, *33*, 46–54. [CrossRef]

47. Rashad, A.M.; Khalil, M.H. A preliminary study of alkali-activated slag blended with silica fume under the effect of thermal loads and thermal shock cycles. *Constr. Build. Mater.* **2013**, *40*, 522–532. [CrossRef]

48. Jiang, H.; Yi, H.; Yilmaz, E.; Liu, S.; Qiu, J. Ultrasonic evaluation of strength properties of cemented paste backfill: Effects of mineral admixture and curing temperature. *Ultrasonics* **2020**, *100*, 105983. [CrossRef] [PubMed]

49. Nath, P.; Sarker, P.K. Effect of GGBFS on setting, workability and early strength properties of fly ash geopolymer concrete cured in ambient condition. *Constr. Build. Mater.* **2014**, *66*, 163–171. [CrossRef]

50. Chen, J.; Kwan, A. Triple Blending with Fly Ash Microsphere and Condensed Silica Fume to Improve Performance of Cement Paste. *J. Mater. Civ. Eng.* **2013**, *25*, 618–626. [CrossRef]

51. Yang, T.; Zhu, H.; Zhang, Z.; Gao, X.; Zhang, C.; Wu, Q. Effect of fly ash microsphere on the rheology and microstructure of alkali-activated fly ash/slag pastes. *Cem. Concr. Res.* **2018**, *109*, 198–207. [CrossRef]

52. Sonebi, M.; Lachemi, M.; Hossain, K.M.A. Optimisation of rheological parameters and mechanical properties of superplasticised cement grouts containing metakaolin and viscosity modifying admixture. *Constr. Build. Mater.* **2013**, *38*, 126–138. [CrossRef]

53. Güllü, H.; Ali Agha, A. The rheological, fresh and strength effects of cold-bonded geopolymer made with metakaolin and slag for grouting. *Constr. Build. Mater.* **2021**, *274*, 122091. [CrossRef]

54. Haiqiang, J.; Fall, M.; Cui, L. Yield stress of cemented paste backfill in sub-zero environments: Experimental results. *Miner. Eng.* **2016**, *92*, 141–150. [CrossRef]

55. Diamond, S.; Sahu, S. Densified silica fume: Particle sizes and dispersion in concrete. *Mater. Struct.* **2006**, *39*, 849–859. [CrossRef]

56. Nochaiya, T.; Wongkeo, W.; Chaipanich, A. Utilization of fly ash with silica fume and properties of Portland cement–fly ash–silica fume concrete. *Fuel* **2010**, *89*, 768–774. [CrossRef]

57. Ma, B.G.; Li, J.Z.; Peng, J. Influence of Mineral Admixtures on Mechanical Properties of High-Performance Concrete. *J. Wuhan Univ. Techno.* **1999**, *14*, 1–7.

58. Kumar, S.; Kumar, R.; Mehrotra, S.P. Influence of granulated blast furnace slag on the reaction, structure and properties of fly ash based geopolymer. *J. Mater. Sci.* **2010**, *45*, 607–615. [CrossRef]

59. Puertas, F.; Martnez-Ramrez, S.; Alonso, S.; Vázquez, T. Alkali-activated fly ash/slag cements: Strength behaviour and hydration products. *Cem. Concr. Res.* **2000**, *30*, 1625–1632. [CrossRef]

60. Fernández, Á.; García Calvo, J.L.; Alonso, M.C. Ordinary Portland Cement composition for the optimization of the synergies of supplementary cementitious materials of ternary binders in hydration processes. *Cem. Concr. Compos.* **2018**, *89*, 238–250. [CrossRef]

61. Alanazi, H.; Hu, J.; Kim, Y.-R. Effect of slag, silica fume, and metakaolin on properties and performance of alkali-activated fly ash cured at ambient temperature. *Constr. Build. Mater.* **2019**, *197*, 747–756. [CrossRef]

62. Bernal, S.A.; Mejía de Gutiérrez, R.; Provis, J.L. Engineering and durability properties of concretes based on alkali-activated granulated blast furnace slag/metakaolin blends. *Constr. Build. Mater.* **2012**, *33*, 99–108. [CrossRef]

63. Bernal, S.A. Carbonatación en Concretos Produci-Dos a Partir de Sistemas Binarios de una Escoria Siderúrgicay un Metacaolin Activados Alcalinamente. Ph.D. Thesis, Universidad del Valle, Cali, Colombia, 2009.

64. Buchwald, A.; Hilbig, H.; Kaps, C. Alkali-activated metakaolin-slag blends—Performance and structure in dependence of their composition. *J. Mater. Sci.* **2007**, *42*, 3024–3032. [CrossRef]

65. Burciaga-Díaz, O.; Escalante-García, J.I.; Arellano-Aguilar, R.; Gorokhovsky, A. Statistical Analysis of Strength Development as a Function of Various Parameters on Activated Metakaolin/Slag Cements. *J. Am. Ceram. Soc.* **2010**, *93*, 541–547. [CrossRef]

66. Tänzer, R.; Buchwald, A.; Stephan, D. Effect of slag chemistry on the hydration of alkali-activated blast-furnace slag. *Mater. Struct.* **2014**, *48*, 629–641. [CrossRef]

67. Burciaga-Díaz, O.; Magallanes-Rivera, R.X.; Escalante-García, J.I. Alkali-activated slag-metakaolin pastes: Strength, structural, and microstructural characterization. *J. Sustain. Cem.-Based Mater.* **2013**, *2*, 111–127. [CrossRef]

68. Rostami, M.; Behfarnia, K. The effect of silica fume on durability of alkali activated slag concrete. *Constr. Build. Mater.* **2017**, *134*, 262–268. [CrossRef]
69. Ramezanianpour, A.A.; Moeini, M.A. Mechanical and durability properties of alkali activated slag coating mortars containing nanosilica and silica fume. *Constr. Build. Mater.* **2018**, *163*, 611–621. [CrossRef]
70. Li, L.; Ali, H.A.; Lu, J.-X.; Poon, C.S. Role of silica fume in alkali-activated slag/glass powder paste. *Constr. Build. Mater.* **2022**, *356*, 129189. [CrossRef]
71. Yılmaz, T.; Ercikdi, B. Predicting the uniaxial compressive strength of cemented paste backfill from ultrasonic pulse velocity test. *Nondestruct. Test. Eval.* **2015**, *31*, 247–266. [CrossRef]
72. Cao, S.; Song, W. Effect of filling interval time on the mechanical strength and ultrasonic properties of cemented coarse tailing backfill. *Int. J. Miner. Process.* **2017**, *166*, 62–68. [CrossRef]
73. Xu, S.; Suorineni, F.T.; Li, K.; Li, Y. Evaluation of the strength and ultrasonic properties of foam-cemented paste backfill. *Int. J. Min. Reclam. Environ.* **2016**, *31*, 544–557. [CrossRef]
74. Yilmaz, T.; Ercikdi, B.; Karaman, K.; Kulekci, G. Assessment of strength properties of cemented paste backfill by ultrasonic pulse velocity test. *Ultrasonics* **2014**, *54*, 1386–1394. [CrossRef]
75. Jiang, H.; Han, J.; Li, Y.; Yilmaz, E.; Sun, Q.; Liu, J. Relationship between ultrasonic pulse velocity and uniaxial compressive strength for cemented paste backfill with alkali-activated slag. *Nondestruct. Test. Eval.* **2019**, *35*, 359–377. [CrossRef]